Uncertainty in Optical Measurement Applications: A Case Study

Markus Brandner, *Member, IEEE*, and Thomas Thurner, *Member, IEEE*

***Abstract*—The uncertainty related to a measurement is at least as important as the measurement itself. Apart from being able to determine intervals of confidence around the final result within which the true measurement value is expected to lie at a certain level of confidence, the rigorous treatment of uncertainty throughout an algorithm allows increasing its robustness against disturbing influences and judging its applicability to a given task. This paper addresses the propagation of uncertainty within a quality control application using image-based sensors. Simulations and real-world results are provided to show the applicability of the proposed application.**

***Index Terms*—Error estimation, optical measurement, range sensor, uncertain geometry, uncertainty propagation.**

I. Introduction

QUALITY control (QC) measurements are one of the most frequently encountered tasks in current industrial measurement applications. Apart from the ever-increasing demand of manufacturing processes with little waste of raw material, the industry is moving toward 100% QC of the produced parts.

Optical measurement systems can meet the requirements of production lines: QC is performed in a fast, robust, and accurate manner in many situations. The requirements on metric accuracy are comparably low for a significant portion of optical QC measurements including color, presence of parts on the conveyor belt, approximative verification of shape, and others. However, there remains a segment of QC measurements that relies on highly accurate metric reconstruction of visual entities. Examples are accurate validation of an object's geometry, measurement of distances and areas, and precise measurements of surface deviations. In the following, we will concentrate on precise measurements of known objects (i.e., with given CAD reference). The high degree of complexity in these vision systems often makes it exceedingly difficult to identify reliable bounds to the measurement uncertainty. Some attempts have been made in the literature to analytically deal with uncertainty in applications that either directly measure properties [1] or need to reason based on the geometry perceived by a vision sensor [2]. The guide to the expression of uncertainty in measurement [3] (GUM) classifies uncertainties according to the method required to handle them into Type A and Type B uncertainty components. In this paper, we discuss the different steps of the design and implementation of an optical QC application with special emphasis on traceable uncertainty propagation of measurement results. The geometric parameters of a large cylinder are estimated using an estimation technique based on the coefficients of the discrete Fourier transform (DFT).

Manuscript received June 28, 2005; revised February 25, 2006.

The authors are with the Institute of Electrical Measurement and Measurement Signal Processing, Graz University of Technology, Graz 8010, Austria (e-mail: brandner@ieee.org; thurner@ieee.org).

Digital Object Identifier 10.1109/TIM.2006.873802

II. Uncertainty in Computer Vision

The extensive application of probability theory to many different tasks in computer vision is largely motivated by the desire to obtain robust algorithms. The incorporation of robust methods enables algorithms to perform the step from "clean" laboratory conditions to "real-world" problems. For an algorithm to be robust against a certain degree of outliers or to be able to be self-validating [4], additional—redundant—information is required. In general, overdetermined systems of equations need to be solved. Coordinates in two-dimensional (2-D) and three-dimensional (3-D) Euclidean space are commonly represented using vectors in $\mathbb{R}^2$ and $\mathbb{R}^3$, respectively. If the underlying geometry is subjected to unknown variations, the coordinates are represented as random vectors $\underline{\mathbf{x}}$. Given the frequently applied Gaussian assumption, the random vector is characterized by

$$\underline{\mathbf{x}} \sim \mathcal{N}(\mu_{\underline{\mathbf{x}}}, \mathbf{\Sigma}_{\underline{\mathbf{xx}}}) \tag{1}$$

where $\mu_{\underline{\mathbf{x}}}$ denotes the mean vector and $\mathbf{\Sigma}_{\underline{\mathbf{xx}}}$ denotes the covariance matrix of the random vector. The transformation of a random vector using a vector-valued function $\mathbf{f}(\cdot)$ results in a new random vector $\underline{\mathbf{y}} = \mathbf{f}(\underline{\mathbf{x}})$, the parameters of which are given by

$$\mu_{\underline{\mathbf{y}}} = \mathbf{f}(\mu_{\underline{\mathbf{x}}}) \tag{2}$$

$$\mathbf{\Sigma}_{\underline{\mathbf{yy}}} = \mathbf{J}(\mathbf{x}) \Sigma_{\underline{\mathbf{xx}}} \mathbf{J}^T(\mathbf{x}) \tag{3}$$

where $\mathbf{J}(\mathbf{x}) = (\partial \mathbf{f}(\mathbf{u})/\partial \mathbf{u})|_{\mathbf{u}=\mathbf{x}}$ denotes the Jacobian of the transformation $\mathbf{f}(\mathbf{x})$ at a given point $\mathbf{x}$. This resultant covariance matrix $\mathbf{\Sigma}_{\underline{\mathbf{yy}}}$ is exact if and only if $\mathbf{f}(\cdot)$ is linear and the higher order terms $\mathcal{O}(\|\Delta\mathbf{x}\|)$ of the Taylor series expansion

$$\mathbf{f}(\mathbf{x}+\Delta\mathbf{x}) = \mathbf{f}(\mathbf{x}) + \left.\frac{\partial \mathbf{f}(\mathbf{u})}{\partial \mathbf{u}}\right|_{\mathbf{u}=\mathbf{x}} \Delta\mathbf{x} + \mathcal{O}\left(\|\Delta\mathbf{x}\|\right) \tag{4}$$

vanish. For a general nonlinear function $\mathbf{f}(\cdot)$, the matrix $\mathbf{\Sigma}_{\underline{\mathbf{yy}}}$ only approximates the true covariance matrix. While numerical methods such as Monte Carlo analysis exist to determine the covariance matrix of the transformed vector, an analytical solution is possible for many transformations encountered in computational geometry.

Apart from uncertainties in coordinates, transformation parameters can be subjected to uncertainty too. Typical scenarios

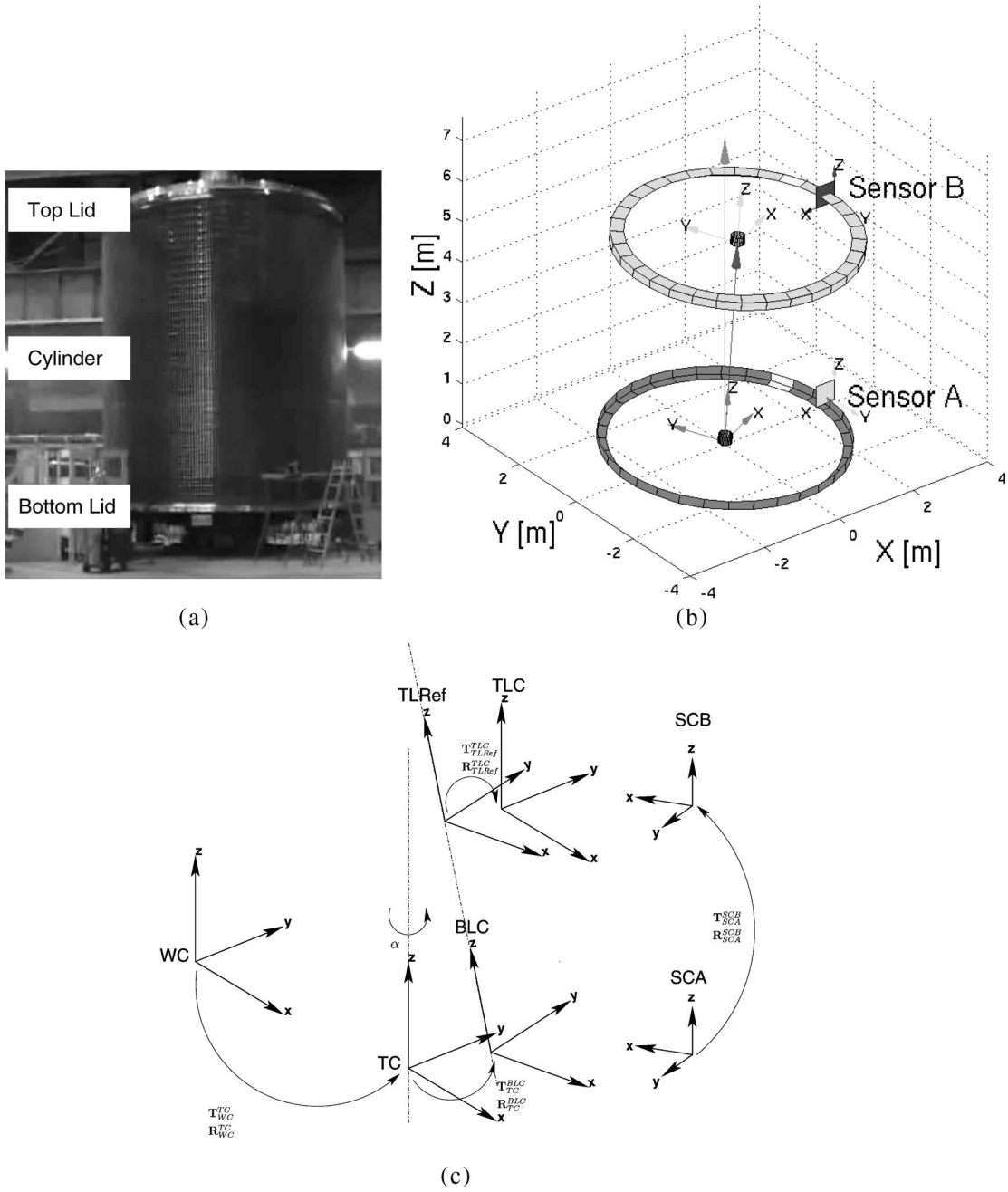

(a) (b) (c)

Fig. 1. Mechanical structure to be verified by the QC application. (a) Image of the structure. The main components (bottom lid, cylinder, and top lid) are clearly visible. (b) Simulation of an imperfectly manufactured cylinder. The top lid exhibits both offset and tilt errors relative to its nominal position and orientation. Two sensors are used by the application: Sensor A mounted at the bottom lid and Sensor B mounted at the top lid. (c) Coordinate systems involved in the measurement process. An overview of the applied assumptions and restrictions is given in Table I.

are uncertain parameters of a calibrated sensor as a result of the calibration process. The rigorous application of first-order uncertainty propagation allows to handle these cases. Consider a linear transformation of a random vector in 3-D

$$\underline{\mathbf{y}} = \mathbf{M} \cdot \underline{\mathbf{x}} \tag{5}$$

which can be rewritten as

$$\underline{\mathbf{y}} = \mathbf{B}_{\underline{\mathbf{x}}} \cdot \underline{\mathbf{m}} \tag{6}$$

where $\mathbf{B}_{\underline{\mathbf{x}}} = \mathbf{I}_3 \otimes \underline{\mathbf{x}}^T$ using the Kronecker symbol. The vector $\underline{\mathbf{m}} = \mathrm{vec}\,(\mathbf{M}^T)$ is a column vector comprising all coefficients of the transformation matrix. If we further denote the covariance matrix of the transformation parameters by $\mathbf{\Sigma}_{\underline{\mathbf{mm}}}$, the transformed random vector can be described by

$$\mu_{\underline{\mathbf{y}}} = \mathbf{M} \cdot \mu_{\underline{\mathbf{x}}} \tag{7}$$

$$\mathbf{\Sigma}_{\underline{\mathbf{yy}}} = \mathbf{B}_{\underline{\mathbf{x}}} \Sigma_{\underline{\mathbf{mm}}} \mathbf{B}_{\underline{\mathbf{x}}}^T. \tag{8}$$

Using the superposition principle allows to combine the two cases to derive the parameters of a Gaussian random vector $\underline{\mathbf{y}}$ that results from transforming a known Gaussian random

vector $\underline{\mathbf{x}}$ using transformation parameters that themselves are subjected to Gaussian variations, i.e.,

$$\boldsymbol{\Sigma}_{\underline{\mathbf{yy}}} = \begin{pmatrix} \mathbf{J} & \mathbf{B}_{\underline{\mathbf{x}}} \end{pmatrix} \begin{pmatrix} \boldsymbol{\Sigma}_{\underline{\mathbf{xx}}} & \boldsymbol{\Sigma}_{\underline{\mathbf{xm}}} \\ \boldsymbol{\Sigma}_{\underline{\mathbf{mx}}} & \boldsymbol{\Sigma}_{\underline{\mathbf{mm}}} \end{pmatrix} \begin{pmatrix} \mathbf{J}^T \\ \mathbf{B}_{\underline{\mathbf{x}}}^T \end{pmatrix}. \tag{9}$$

Note that using Euclidean coordinate vectors as indicated above does not permit us to deal with pure translations in a similar framework. However, the straightforward extension of a coordinate vector in $\mathbb{R}^n$ by a nonzero homogeneous coordinate leads to the representation of the point in homogeneous coordinates within the projective space $\mathbb{P}^n$ within which all allowed Euclidean transformations are representable in the form of (5). The presented relations provide a basic tool for rigorous first-order uncertainty propagation in signal processing chains provided that the underlying processes are indeed Gaussian and the uncertainty introduced by the implicit linearization using Jacobian matrices is negligible.

III. Optical QC

In the subsequent section, we present a system for optical QC measurements on large rotationally symmetric structures. In particular, the application targets cylinders with up to 6 m in height and 5.5 m in diameter. Critical parameters of the structure are the alignment of the top and bottom lid (both relative to the cylinder axis and relative to each other). Given restrictions during the manufacturing process, only parts of the outer surfaces of both the bottom and the top lids of the cylinder can act as metric references. Fig. 1(a) and (b) depicts a close-up of the cylinder taken during a measurement and a sketch of the setup consisting of the cylinder represented by two lids and two sensors, respectively. As a consequence of cylinder manufacturing, the following conditions apply:

1) It cannot be guaranteed that both the top and the bottom lids are perfect discs. Deviations from the nominal radius along the circumference and nonplanarity are encountered.
2) In order to access the cylinder, it is vertically mounted on a turntable. Both the position of the cylinder on the turntable and the orientation of the turntable axis are subjected to unknown—but constant—deviations.
3) Measurements shall be performed during the whole production process as to apply corrections upon notification of manufacturing flaws. Therefore, the measurement apparatus must be attached in such a way that it is not influenced by ongoing work on the cylinder and that it itself does not prevent manufacturing.

The different coordinate systems and variables of the proposed QC application are outlined in Fig. 1(c); their description is given in Table I. For a general constellation (i.e., $T_{TC}^{BLC} \neq \mathbf{0}$, $R_{TC}^{BLC} \neq \mathbf{I}$), the signals captured by the two 2-D range sensors are periodic sinusoids parameterized by the displacement of the respective lid as indicated by the simulation shown in Fig. 5(a). This holds both for measurements in the direction of the x-axis (perpendicular to the cylinder axis) and for deviations in the direction of the z-axis (parallel to the cylinder axis).

TABLE I
Overview of the Different Coordinate Systems and Variables Associated With the Setup

WC	world coordinate system
TC	turn table coordinate system
BLC	bottom lid coordinate system
$TLRef$	top lid reference coordinate system
TLC	top lid coordinate system
H	height of the cylinder
R	lid radius
R_{WC}^{TC},T_{WC}^{TC}	rotation and translation $WC \rightarrow TC$
R_{TC}^{BLC},T_{TC}^{BLC}	rotation and translation $TC \rightarrow BLC$
R_{TLRef}^{TLC},T_{TLRef}^{TLC}	rotation and translation $TLRef \rightarrow TLC$

The maximum misalignment of the cylinder on the turntable and the maximum deviation of the turntable axis from the normal are bound by the manufacturer to be small compared to the radius R of the lids ($\|T_{TC}^{BLC}\| \ll R$). Thus, the cross-sensitivities of lid tilts to offset measurements and lid offsets to tilt measurements are bound and—for this setup—can be neglected. We denote our target measurements as tilt R_{TLRef}^{TLC} and offset T_{TLRef}^{TLC} as indicated in Fig. 1(c). The rotational and translational parameters R_{WC}^{TC}, T_{WC}^{TC}, R_{TC}^{BLC}, and T_{TC}^{BLC} are unknown but assumed to be constant during the measurement process.

A. Sensor Devices

The proposed QC application requires to measure the position of the upper and lower lid circumferences with respect to an upper and a lower sensor coordinate system, respectively. In addition, the application requires to measure the current angular position α [cf. Fig. 1(c)] of the turntable simultaneously with the range sensor readings. The angular position of the cylinder is measured using a camera that points toward the outer surface of the cylinder. Periodic structures on the cylinder and regularly spaced unique optical markers in conjunction with a constant rate of rotation allow to accurately determine the current position of the turntable. The test measurement setup was used to take 1500–2500 measurements during a single rotation of the cylinder. The obtained expanded uncertainty of the angular position measurement is $U_\alpha = 0.02^\circ$ ($k = 3$, 99.74% level of confidence) so that its influence to the final measurement result can be neglected. The position of the lid reference surfaces is measured using two 2-D range sensors that are positioned next to the rotating cylinder as indicated by the two coordinate systems Sensors A and B in Fig. 1(b). Each sensor consists of a semiconductor laser module projecting a line onto the lid reference planes, a camera observing the area of intersection, and an optional set of accelerometers to monitor vibrations of the sensor platform [cf. Fig. 2(a) for a close-up of the final sensor in operation without attached acceleration sensors]. A detailed description of the range sensor design and associated signal processing algorithms is given in [5]. However, the important steps are repeated here to provide the reader with insights important to the understanding of the uncertainty propagation process. Using a precision macrolens, the active sensing area of the setup is 12×10 mm^2, corresponding to captured images of 644×492 pixel^2. The sensor principle is as follows: The

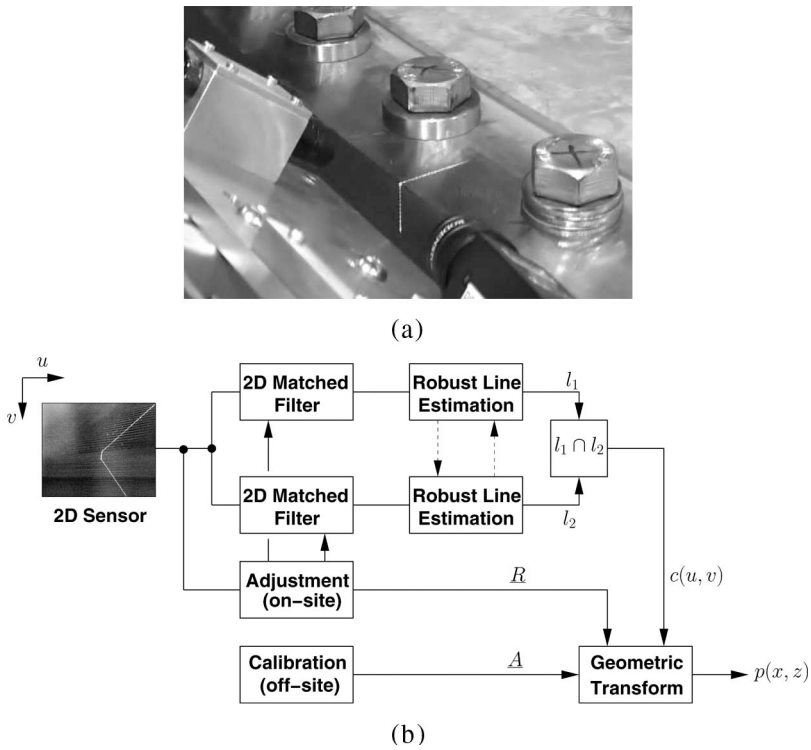

Fig. 2. (a) Close-up of the 2-D range sensor hardware. (b) Signal processing involved in the sensor front-end. Robust line estimation algorithms are applied to the acquired image. Matched filters using *a priori* setup information increase the robustness of the sensor with respect to ambient illumination and surface imperfections.

projected line intersects with the respective reference planes resulting in two perpendicular lines captured by the camera. The sequence of images acquired during a single turn of the turntable is processed by an algorithm as outlined in Fig. 2(b). Using *a priori* geometric information about the reference planes (given by the CAD model of the lids), two optimal filters are used to increase the signal-to-noise ratio (SNR) of the sensor's input signal. Each of these 2-D matched filters is adjusted to its respective target line of intersection. Parameters to be tuned are filter width and filter orientation assuming a Gaussian intensity profile across the lines. A robust line estimation algorithm is applied to estimate both sets of line parameters for l_1 and l_2, respectively. The point $c(u, v)$ in image coordinates results from intersecting the lines and denotes the position of the lid circumference at the current angular position α of the turntable. A calibration process performed under laboratory conditions using a dedicated calibration target and an on-site adjustment process result in the parameters of the homography matrix $\mathbf{A}$ and the rotation matrix $\mathbf{R}$.

In order to determine the uncertainty of the sensor's measurement setup, the following sources of uncertainty have to be considered.

- Uncertainty of the image processing algorithms: The position of the intersection point $c(u, v)$ is subjected to random variations. Possible causes for these variations are different noise sources within the camera and the acquisition hardware, mismatch of the reference surface model (e.g., deviations from the true planar surfaces), nonconstant illumination (e.g., reflections, changes in ambient light), and sensor vibrations.
- Prior to the measurement, the sensor has to be calibrated (off-site) and adjusted with respect to the actual cylinder (on-site). Both operations are subjected to uncertainties due to, e.g., imperfections of the calibration target and its positioning during the calibration process, and image processing uncertainties as described in the previous point causing deviations during calibration and adjustment.

Subsequently, we will follow the procedure suggested by the GUM [3] to determine the overall uncertainty of the QC system, taking into account both the uncertainty introduced by the sensor calibration and the uncertainties introduced during the measurement process.

1) Sensor Calibration: During the calibration process of the sensor, the calibration target is positioned at discrete points within the sensing area using a 2-D microtranslator setup. Based on the known position of the distinct points on the calibration target and their corresponding points measured in the camera image, the eight degrees of freedom 2-D homography $\mathbf{A}$ is estimated using the normalized direct linear transform method [6]. The homography affects the overall uncertainty of the sensor in two ways. First, the parameters of the homography are estimated in a least-squares sense. For a general calibration scenario, the underlying system of equations is overdetermined leading to residual errors spread over the whole set of input points. Second, the parameters of the homography itself are subjected to variations once both model points (i.e., the positions of the calibration target) and test points (i.e., the points measured in the image) are uncertain. In this case, one can associate a 9×9 covariance matrix $\Sigma_{\underline{\mathbf{hh}}}$ to the homography characterizing its uncertainty up to the first order.

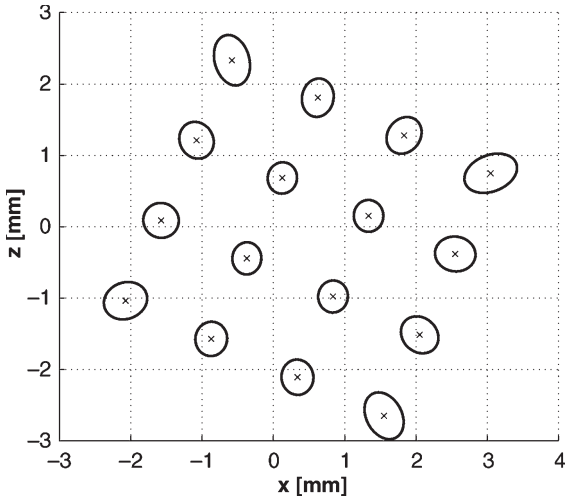

Fig. 3. Regions of confidence within the central area of the sensor. $N = 10^5$ Monte Carlo runs were performed to estimate the covariance matrices of a set of mapped image points. The uncertainty in this image is caused by both uncertain homography parameters and uncertain input points. The maximum variance within the target area of the sensor is bound to $\sigma^2_{\text{Position}} \leq 1.606 \cdot 10^{-7}$ mm^2. Note that the variances have been scaled considerably for visualization purposes.

In order to increase the accuracy of the calibration, we restrict the working area of the sensor to an approximately 5×5 mm^2 field around the center of the camera. This area is subsequently referred to as center area A_{center}. The homography parameters for the proposed sensor are determined as follows. During an experiment, pairs of model and test points are generated using the calibration target as described above. Given the specification of the microtranslator devices, a conservative estimate of the positioning uncertainty $\sigma^2_{\text{Position}} \leq 1.089 \cdot 10^{-7}$ mm^2 has been identified. The empirical covariance of the $p(x, z)$ estimates is found using $N = 100$ sensor readings per target position. The maximum of the obtained variances (i.e., the largest eigenvalue of all covariance matrices) was found to be $\sigma^2_{\text{Image}} \leq 0.0139$ pixel^2 within A_{center}. Using this information, $N = 10^5$ Monte Carlo runs using the above covariances have been performed to estimate the covariance matrix of the homography parameters. The mean homography parameters are used to determine the residual error that in this case is bound to 19.6 μm. Fig. 3 depicts the regions of confidence within which a certain percentage of the projected image points lie. The associated covariances have been scaled for visualization purposes. The increasing size of the confidence intervals (i.e., the variances of the projected points increase with the distance from the image center) supports the choice of a restricted working area A_{center}. If, in addition to uncertainty in the homography parameters, the input points are subjected to random variations, (9) can be used to analytically derive the resulting covariance matrices. Our setup results in a maximum covariance of $\sigma^2_{\text{Position}} \leq 1.606 \cdot 10^{-7}$ mm^2 within A_{center}. In order to verify the validity of the first-order uncertainty propagation introduced in Section II, the sensor signals have been investigated according to their statistical properties. Fig. 4 depicts normalized quantile plots of the x- and z-sensor signals' real-world input data. Both distributions approach the Gaussian distribution justifying the first-order propagation of uncertainties as proposed above. Assuming that 99.74% of the residuals lie within the given boundary, we compute the combined uncertainty for this sensor within the center area A_{center} to be

$$u_c^2(x) = u^2_{\text{Transformation}}(x) + u^2_{\text{Residual}}(x) \tag{10}$$

$$= 4.28 \cdot 10^{-5} \text{ mm}^2. \tag{11}$$

The same result applies to $u_c^2(z)$ for symmetry reasons. The expanded uncertainty is given by

$$U = k \cdot u_c(x) = 3.0 \cdot 6.54 \cdot 10^{-3} = 1.962 \cdot 10^{-2} \text{ mm} \tag{12}$$

for a level of confidence of 99.74% (3σ interval of confidence).

B. Estimation of Lid Parameters

Due to its periodic nature, $x[n]$ can be rewritten as

$$x[n] = \sum_{k=0}^{N-1} a_k \cos\left[\frac{2\pi kn}{N}\right] + \sum_{k=0}^{N-1} b_k \sin\left[\frac{2\pi kn}{N}\right] + w[n] \tag{13}$$

using superposition of N harmonically related sinusoids of frequencies $\omega_k = 2\pi k/N$. Based on this signal model, we apply a DFT that results in the minimum variance unbiased estimators (MVUE) $\hat{a}_k$ and $\hat{b}_k$ for amplitudes a_k and b_k of a sinusoidal signal embedded in additive white Gaussian noise [7]. The phase of the signal buried in Gaussian noise can be estimated using

$$\hat{\phi}_k = -\arctan \frac{\sum_{n=0}^{N-1} b_k \sin\left[\frac{2\pi kn}{N}\right]}{\sum_{n=0}^{N-1} a_k \cos\left[\frac{2\pi kn}{N}\right]} \tag{14}$$

which is the approximate maximum likelihood estimator (MLE) [7]. The variances of these estimators are given by

$$\text{var}(\hat{a}_k) = \text{var}(\hat{b}_k) = \frac{2\sigma^2_{\text{Noise}}}{N} \tag{15}$$

$$\text{var}(\hat{\phi}) = \frac{2\sigma^2_{\text{Noise}}}{N \cdot a^2} \tag{16}$$

where a denotes the amplitude of the signal.

C. Estimating Offset and Tilt

In the sequel, we denote the offset of a lid with respect to its ideal position by $\boldsymbol{\Delta}$ and subscripts A and B for the bottom and top sensors, respectively, as shown in Fig. 1(b). The angle of the offset vector will be denoted by θ. Similarly, the tilt of a lid is expressed by a tilt vector $\boldsymbol{\Gamma}$ and its associated angular position within the lid plane φ. The discrete time sensor signals are given by $x_A[n]$ and $z_A[n]$ for the bottom sensor and $x_B[n]$ and $z_B[n]$

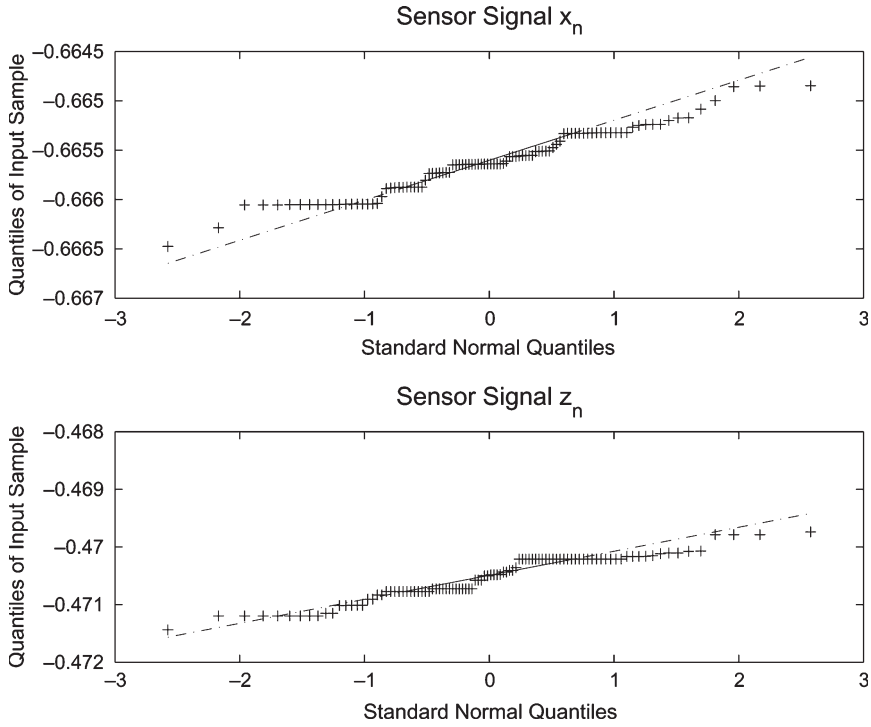

Fig. 4. Quantile plots of the sensor's x (upper figure) and z (lower figure) signals. Deviations from the reference Gaussian indicate slightly long-tailed distributions.

for the top sensor, respectively. Assuming that $\|\mathbf{\Delta}_A\| \ll R$ and $\|\mathbf{\Delta}_B\| \ll R$, the sensor signals can be written as

$$x_A[n] \approx c_1 - \|\mathbf{\Delta}_A\| \cos\left[\frac{2\pi}{N}n + \theta_A\right] + w_1[n] \quad (17)$$

$$z_A[n] \approx c_2 + \|\mathbf{\Gamma}_A\| \cos\left[\frac{2\pi}{N}n + \varphi_A\right] + w_2[n] \quad (18)$$

$$x_B[n] \approx c_3 - \frac{H}{R}\|\mathbf{\Gamma}_A\| \cos\left[\frac{2\pi}{N}n + \varphi_A\right] \quad (19)$$

$$- \|\mathbf{\Delta}_A\| \cos\left[\frac{2\pi}{N}n + \theta_A\right] \quad (20)$$

$$- \|\mathbf{\Delta}_B\| \cos\left[\frac{2\pi}{N}n + \theta_B\right] + w_3[n] \quad (21)$$

$$z_B[n] \approx c_4 + \|\mathbf{\Gamma}_A\| \cos\left[\frac{2\pi}{N}n + \varphi_A\right] \quad (22)$$

$$+ \|\mathbf{\Gamma}_B\| \cos\left[\frac{2\pi}{N}n + \varphi_B\right] + w_4[n] \quad (23)$$

where the signals $w_i[n]$ denote independent noise components. All sensor signals consist of a phase-shifted sinusoid with frequency $(2\pi/N)n$. By coefficient comparison, we obtain

$$\hat{a}_{\mathbf{\Delta}_B} = -\frac{H}{R}\hat{a}_{z_A} - \hat{a}_{x_A} - \hat{a}_{x_B} \quad (24)$$

$$\hat{b}_{\mathbf{\Delta}_B} = -\frac{H}{R}\hat{b}_{z_A} - \hat{b}_{x_A} - \hat{b}_{x_B} \quad (25)$$

$$\hat{a}_{\mathbf{\Gamma}_B} = \hat{a}_{z_B} - \hat{a}_{z_A} \quad (26)$$

$$\hat{b}_{\mathbf{\Gamma}_B} = \hat{b}_{z_B} - \hat{b}_{z_A} \quad (27)$$

where the c_is are setup-dependent constants, $\hat{\mathbf{\Delta}}_B = (\hat{a}_{\mathbf{\Delta}_B}, \hat{b}_{\mathbf{\Delta}_B})^T$ denotes the estimated top lid offset vector, and $\hat{\mathbf{\Gamma}}_B = (\hat{a}_{\mathbf{\Gamma}_B}, \hat{b}_{\mathbf{\Gamma}_B})^T$ denotes the estimated top lid tilt vector. Since all contributing variables are subjected to Gaussian deviations, the combined uncertainties of the estimation results are given by

$$u^2_{c,\hat{a}_{\mathbf{\Delta}_B}} = u^2_{c,\hat{b}_{\mathbf{\Delta}_B}} = u^2_{c,(\hat{a},\hat{b})}\left[(H/R)^2 + 2\right] \quad (28)$$

$$u^2_{c,\hat{a}_{\mathbf{\Gamma}_B}} = u^2_{c,\hat{a}_{\mathbf{\Gamma}_B}} = 2u^2_{c,(\hat{a},\hat{b})} \quad (29)$$

where $u^2_{c,(\hat{a},\hat{b})}$ denotes the combined uncertainty of the estimates $\hat{a}_1$ and $\hat{b}_1$, respectively. The final measurement results $\hat{\mathbf{\Delta}}_B$ and $\hat{\mathbf{\Gamma}}_B$ now exhibit Rayleigh-distributed deviations $\mathcal{R}(\sigma^2)$ of the amplitude and uniformly distributed orientations. Thus, the combined uncertainty for N measurements around the lid is given by

$$u^2_c\left(\|\mathbf{\Delta}_B\|\right) = 6.65 \cdot 10^{-4}\frac{1}{N}\ \text{mm}^2 \quad (30)$$

$$u^2_c\left(\|\mathbf{\Gamma}_B\|\right) = 9.844 \cdot 10^{-5}\frac{1}{N}\ \text{mm}^2 \quad (31)$$

$$u^2_c(\theta) = 8.56 \cdot 10^{-5}\frac{1}{N\|\mathbf{\Delta}_B\|^2}\ \text{rad}^2 \quad (32)$$

$$u^2_c(\varphi) = 8.56 \cdot 10^{-5}\frac{1}{N\|\mathbf{\Gamma}_B\|^2}\ \text{rad}^2. \quad (33)$$

IV. Results

Fig. 5(b) and (c) shows the four sensor signals acquired during an on-site QC measurement. Although the first harmonics are in agreement with the simulation results, significant higher order harmonics are present especially in z signals. These harmonics are due to nonplanar lid elements. In fact,

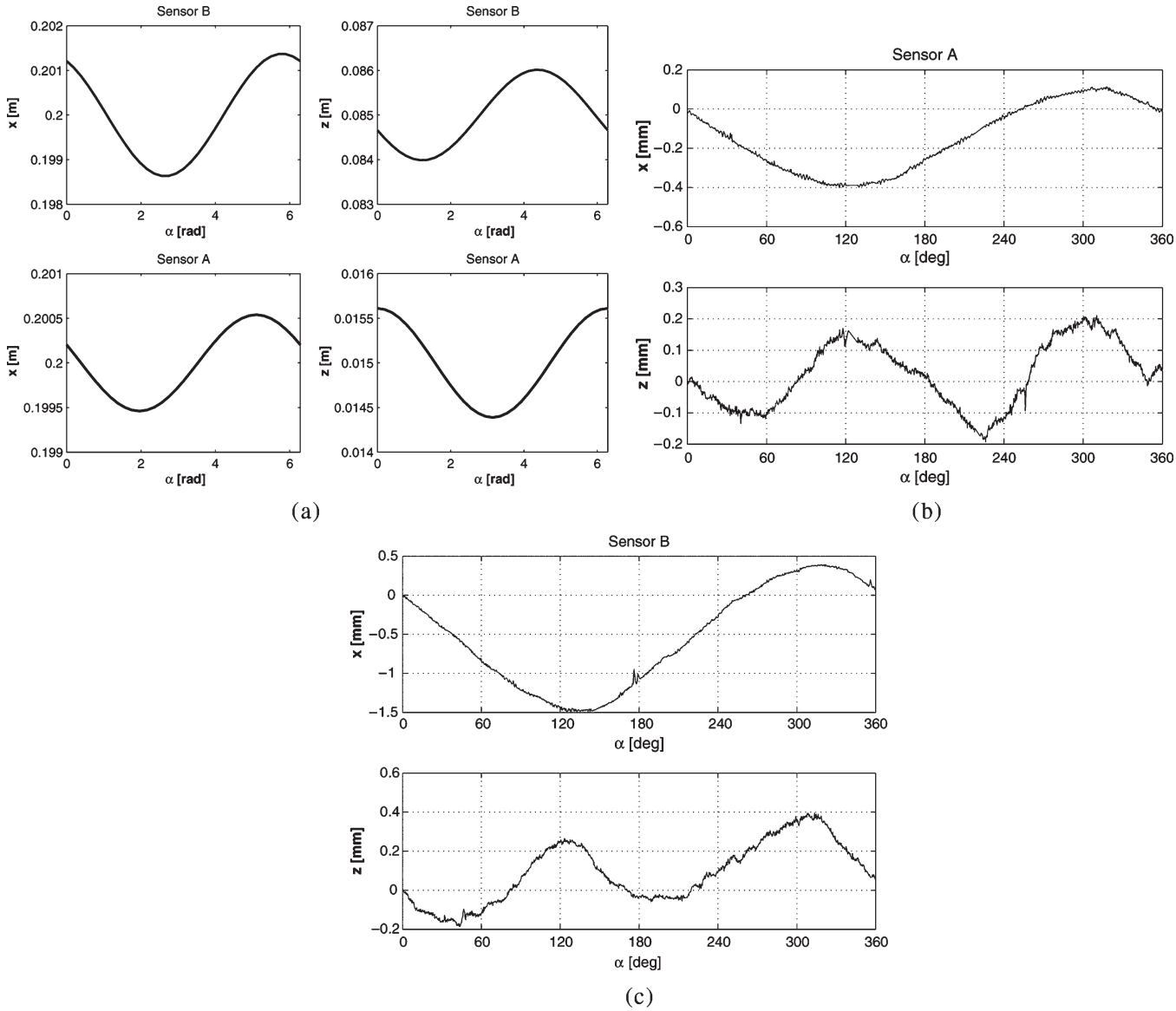

Fig. 5. Sensor data. (a) Simulation of a full cylinder rotation. (b) and (c) Sensor signals obtained during a QC measurement. Note the strong second-order harmonics in the z signals that result from nonplanar lid elements with a sensor setup as shown in Fig. 1(b).

the cylinder was supported by four arms at positions of 0°, 90°, 180°, and 270°. The measurement results using a level of confidence of 99.74% ($k = 3$) and $N = 1500$ are

$$\|\mathbf{\Delta}_B\| = (0.616 \pm 2 \cdot 10^{-3})\ \text{mm}$$
$$\theta = (2.33 \pm 0.001)\ \text{rad}$$
$$\|\mathbf{\Gamma}_B\| = (0.087 \pm 8 \cdot 10^{-4})\ \text{mm}$$
$$\varphi = (4.626 \pm 0.008)\ \text{rad}.$$

The uncertainty budget covering expanded uncertainties at different processing steps of the QC application is summarized in Table II.

TABLE II
EXPANDED UNCERTAINTY BUDGET OF THE QC MEASUREMENT. ELEMENTS ARE BASED ON A LEVEL OF CONFIDENCE OF 99.74%

Line Intersection	$U_{u,v} = 0.35$ pixel
Sensor Calibration	$U_{x,z} = 19.62\,\mu$m
Lid Offset	$U_{\mathbf{\Delta}_B} = 1.75\,\mu$m
	$U_\theta = 1$ mrad
Tilt	$U_{\mathbf{\Gamma}_B} = 0.8\,\mu$m
	$U_\varphi = 8$ mrad

V. CONCLUSION

In this paper, we discuss the issue of uncertainty propagation in optical measurement applications. A QC setup is presented, and the assumptions and specifications of the system components are addressed with respect to their influence on the overall uncertainty of the measurement result. Simulations show the principal functionality of the application, and a real-world measurement indicates the feasibility of the proposed measurement setup to fulfill the requested QC task. The expanded uncertainties and the corresponding levels of confidence of the final results are given.

REFERENCES

[1] K. Kanatani, "Gauges and gauge transformations for uncertainty description of geometric structure with indeterminacy," *IEEE Trans. Inf. Theory*, vol. 47, no. 5, pp. 2017–2028, Jul. 2001.

[2] S. Heuel, *Uncertain Projective Geometry: Statistical Reasoning for Polyhedral Object Reconstruction*, vol. 3008, Lecture Notes in Computer Science. New York: Springer-Verlag, 2003.

[3] International Organization for Standardization (ISO), *Guide to the Expression of Uncertainty in Measurement*, 1995.

[4] W. Förstner, "The role of robustness in computer vision," in *Vis. Milest.*, A. Pinz, W. Burger, Eds., Stift Vorau, Austria, Mar. 1995, pp. 61–74. Österreichische Gesellschaft für Artificial Intelligence.

[5] M. Brandner and T. Thurner, "Robust high-precision 2d optical range sensor," in *Proc. SPIE—Optical Metrology*, Munich, Germany, 2005, pp. 327–335.

[6] R. I. Hartley and A. Zisserman, *Multiple View Geometry in Computer Vision*, 2nd ed. Cambridge, U.K.: Cambridge Univ. Press, 2004.

[7] S. M. Kay, *Fundamentals of Statistical Signal Processing: Estimation Theory*, vol. 1. Englewood Cliffs, NJ: Prentice-Hall, 1993.

Markus Brandner (M'05) received the M.S. degree in telematics (computer engineering) from Graz University of Technology, Graz, Austria, in 1999.

His research interests include statistical signal processing, optical measurement principles, and real-time optical tracking systems.

Thomas Thurner (M'03) received the M.Sc. and Ph.D. degrees in electrical engineering from Graz University of Technology, Graz, Austria, in 1999 and 2005, respectively.

In 2000, he was a University Assistant in the field of measurement science at the Institute of Electrical Measurement and Measurement Signal Processing, Graz University of Technology. His research interests are optical measurement principles and measurement signal processing.